Design and Experimental Analysis of a New Magnetically Levitated Tubular Linear Actuator

S. Miric,
P. Küttel,
A. Tüysüz,
J. W. Kolar

Design and Experimental Analysis of a New Magnetically Levitated Tubular Linear Actuator

Spasoje Mirić, *Student Member, IEEE*, Pascal Küttel, Arda Tüysüz,
and Johann W. Kolar, *Fellow, IEEE*

Abstract—The usage of tubular linear actuators (TLAs) in direct-drive systems where linear reciprocal motion is needed is beneficial compared to systems where a rotational actuator is used together with a mechanical transmission. Systems with TLAs are more compact, more dynamic and more reliable. Today's TLAs commonly employ mechanical or air bearings, which either result in friction and wear due to contact, or a costly and bulky system due to the external pressurized air supply. These issues can be avoided with magnetic bearings (MBs). In literature, it has been proposed to use two separate MBs on each axial side of the TLA, but this approach leads to a longer shaft and a more complex overall system due to additional power and control electronics for the MBs. Therefore, this paper proposes an integration of MBs into the TLA, resulting in a new, self-bearing (bearingsless) TLA. The proposed system is derived from the standard TLA, by changing its stator geometry. The principle of operation is explained and key design aspects are studied using FEM. A prototype integrated into a test bench is built, and used for experimentally verifying the design of the novel actuator.

Index Terms—Bearingless, Linear Motor, Magnetic Levitation, Self-bearing, Tubular Linear Actuator.

I. INTRODUCTION

TUBULAR linear actuators (TLAs) offer certain benefits compared to flat linear actuators such as better exploitation of the permanent magnet (PM) flux, absence of unsymmetric attractive forces between the stator and the mover, and higher power density [1]. Therefore, there is a growing trend in using TLAs in many versatile applications such as pick-and-place robots used in packaging lines or very precise component mounting on printed circuit boards [2], [3], surgery robots [4], [5], active suspension of vehicles [6], electrical power generation [7]–[9], linear compressors [10]–[12] and walking robots [13]. Because of their closed form, TLAs are also convenient for underwater [14] or high-purity applications [15].

Bearings used in TLAs today are mainly mechanical bearings. These bearings feature drawbacks such as friction, risk of
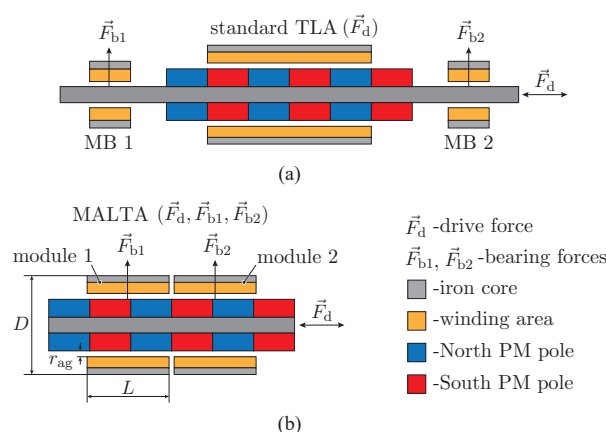
Fig. 1. Magnetic support of the mover in TLA: (a) with two standalone MBs and (b) the proposed MALTA.

contamination due to wear and limited lifetime [16]. Moreover, their use in high-accuracy positioning systems is limited due to thermal disturbance. In order to overcome some of these issues, higher-end TLAs feature air bearings, which, on the other hand, increase system complexity since a pressurized air supply is necessary. Moreover, air bearings prohibit operation in vacuum.

Even though magnetic bearings (MBs) would overcome the issues mentioned earlier, their integration into a TLA system has not been analyzed thoroughly in literature. In [17], a system with two standalone MBs used at each axial end of a TLA is analyzed, see Fig. 1(a). This system, compared to the standard TLA, is characterized by a bulkier design, a higher complexity and a longer mover.

In this paper, the integration of MBs into the TLA, which results in a magnetically levitated tubular actuator (MALTA), is analyzed and an actuator prototype is built. The concept is illustrated in Fig. 1(b). The MB integration is achieved by introducing slits in the circumferential direction in the teeth of the standard TLA stator, which are normally not interrupted in the circumferential direction. A new winding arrangement is proposed, which can alter the air gap magnetic field distribution both in the circumferential and axial directions. This is achieved by replacing the circumferentially uninterrupted coils of a standard TLA with concentrated windings wound around the teeth, which are now separated by the newly introduced slits. The proposed MALTA features lower mass and inertia

of the moving parts and higher compactness compared to a standard TLA with additional MBs. Even though the detailed discussion of the suitable control strategies is not the topic of this paper, the actuator design is carried out with a controlled magnetic levitation in mind. For instance, in order to control the tilting of the mover, the stator of the MALTA consists of two modules (module 1 and module 2, see Fig. 1(b)) that can generate two independent bearing forces ($\vec{F}_{b1}$ and $\vec{F}_{b2}$). Moreover, design aspects affecting the levitation controller, such as the radial pull force and the circumferential dependency of the bearing force constant are also studied.

The principle of operation of the MALTA and its derivation from a standard TLA are discussed in Sec. II. Sec. III details key design aspects of the proposed actuator topology. A prototype embedded in a purpose-built test bench is shown in Sec. IV. Measurement results are compared with FEM simulations and reported in Sec. V. Sec. VI concludes the paper and gives an outlook.

II. PRINCIPLE OF OPERATION

The derivation of the MALTA from the standard TLA and its principle of operation are explained in this section. In Fig. 2(a) the standard, 3-phase TLA drive windings are shown and denoted as L_1, L_2 and L_3. In order to generate the drive force, currents in the TLA drive windings are equal to

$$i_k^d(t) = I_m^d \cos\left(\theta_d(t) + (k-1)2\pi/3\right), \qquad (1)$$

where $\theta_d(t)$ is the mover's electrical axial position at time t and $k \in \{1,2,3\}$ denotes the phase. With these windings, the flux density in the air gap of the TLA can be altered only in axial direction. Consequently, it is not possible to control the bearing (radial) force on the mover. Accordingly, a rearrangement of the standard TLA winding geometry is required such that the control of the air gap flux density in circumferential direction is possible, which allows the generation and control of a bearing force. The winding arrangement, which can control both the drive and the bearing forces is shown in Fig. 2(b). These windings can be interpreted as a combination of 3-phase drive windings and 3-phase heteropolar MB windings.
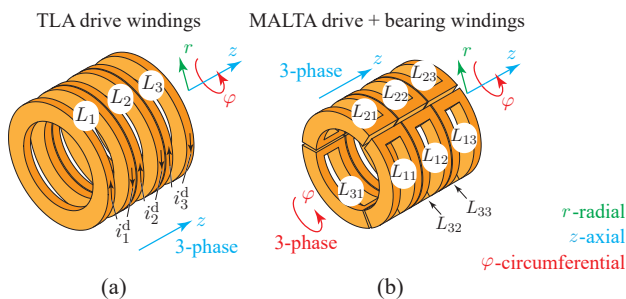

Fig. 2. Schematic representation of the evolution of the MALTA from the standard TLA. (a) Standard TLA windings. (b) MALTA windings with combined drive and bearing force generation capability.

In order to generate drive and bearing forces with the single set of the MALTA windings (see Fig. 2(b)), the phase current is a superposition of the drive and the bearing current components, i.e. the current of the L_{jk} winding is equal to

$$i_{jk}(t) = i_{jk}^d(t) + i_{jk}^b(t), \qquad (2)$$

where $j,k \in \{1,2,3\}$, i_{jk}^d and i_{jk}^b are drive and bearing current components, respectively. The drive current component is supposed to generate only the drive force and the bearing force is generated only with the bearing current component, i.e. these two current components provide a decoupled control of the drive and bearing forces.

Equal phase currents in all the MALTA windings at the same axial position will provide zero bearing force. Therefore, the drive current component of the winding L_{jk} is equal to

$$i_{jk}^d(t) = i_k^d(t), \qquad (3)$$

where i_k^d is from (1). Generating only the bearing force is more complex, as it depends on the bearing force circumferential direction and mover's axial position. Therefore, the current in the winding L_{jk} is modulated both, in circumferential and axial directions as

$$i_{jk}^b(t) = \quad I_m^b \cos\left(\varphi + (j-1)2\pi/3\right) \times \\ \cos\left(\theta_d(t) + (k-1)2\pi/3 + \pi/2\right), \qquad (4)$$

where $j,k \in \{1,2,3\}$ and φ is the bearing force circumferential direction. The argument in the second cos-function of (4), related to the axial electrical angle, is shifted by $\pi/2$ compared to the argument in (1). This ensures zero drive force when a bearing force is commanded, i.e. a decoupled control of the drive and the bearing forces in the MALTA. A similar method for a decoupled control of two mechanical quantities with a single set of windings by modulating the phase currents in the circumferential and axial directions is explained in [18] and [19]. Even though the actuator in those papers is a linear-rotary actuator with no MBs (the controlled mechanical quantities are rotational torque and axial force, rather than radial and axial forces), the presented decoupled control method is applied here for the control of drive and bearing forces.

For allowing a tilting control of the mover, the MALTA consists of two modules (module 1 and module 2, see Fig. 1(b)) equipped with the windings from Fig. 2(b).

III. MACHINE DESIGN

Key design aspects of the MALTA are addressed in this section. By choosing the key geometry parameters, the goal of the design is to maximize the axial and the bearing forces and to minimize the mover mass, i.e. to maximize the axial and sustainable radial accelerations[1].

The constraints in the MALTA design are the outer dimensions, radial air gap size and material properties as summarized in Tab. I. Additionally, practical limitations such as simple manufacturing of windings, off-the-shelf available PM shapes, easily accessible and machinable core materials are all boundaries that are considered in this design.

[1]A linear actuator can be mounted on a kinematic system that moves it radially with high accelerations. This translates into a sustainable radial acceleration, i.e. a MB force requirement that depends on the mover's mass and the acceleration of the whole MALTA in the radial direction.

TABLE I
MALTA DESIGN CONSTRAINTS.

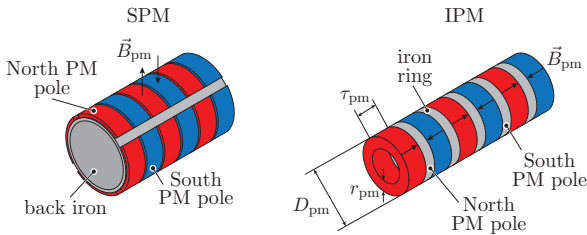| Symbol	Quantity	Value
geometrical		
L	module active length	60 mm
D	stator diameter	60 mm
r_{ag}	air gap radial size	2 mm
materials		
-solid steel CK45 used as iron core material		
μ_r	relative permeability	500
B_{max}	saturation flux density	1.3 T
-neodymium PM used in the mover		
B_r	PM remanent flux density	1.18 T
-copper used for windings		
σ_{Cu}	copper conductivity (20 °C)	58.5 S m^{-1}

Fig. 3. SPM and IPM mover.

FEM is used in the design procedure. The reason why analytical models are not used is they are usually developed in cylindrical coordinate systems and do not account for radial displacement, i.e. cannot calculate the radial pull force.

A. Mover Design

Two different mover configurations are considered in the design procedure, i.e. surface-mounted PMs (SPM) and interior PMs (IPM), as shown in Fig. 3. The SPM mover consists of PMs magnetized in radial direction, as denoted with arrows pointing radially outwards (North PM pole) and radially inwards (South PM pole). In the IPM mover type, PMs are magnetized axially. Therefore, the iron rings are used to form the poles in this mover type.

The considered PM dimensions are given in Tab. II. These PMs define different mover geometries, and each of them is evaluated with two 3D FEM magnetostatic simulations, one for axial force (currents are set according to (3)), and one for bearing force (currents are set according to (4)). Axial and sustainable radial accelerations are calculated in post processing based on the obtained forces. No additional load is considered, i.e. the actuator is used only for levitating and accelerating its mover, which is a very reasonable assumption e.g. considering the use of MALTA in pick-and-place robots in semiconductor industry, where the mass of the potential load is negligible compared to that of the mover itself. The forces are determined by the electrical loading, which is limited by the maximum allowed winding temperature and the actuator's thermal properties. In order to provide quantitative results, the electrical loading is set such that mean copper losses are 15 W, which is based on a simplified thermal model that is given in [20] for an actuator with similar outer dimensions.

TABLE II
CONSIDERED PMs FOR THE MOVER DESIGN

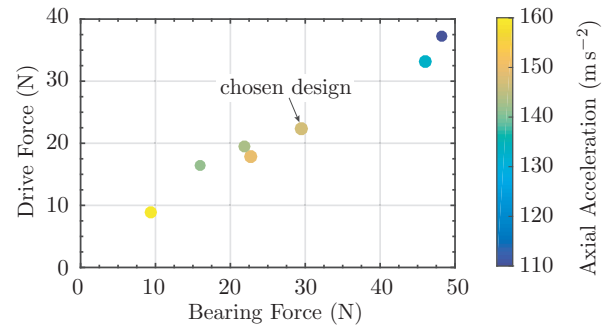| Pole Size	D_{pm}	r_{pm}	τ_{pm}
SPM (radially magnetized PMs)			
10 mm	35.75 mm	1.5 mm	9 mm
7.5 mm	22.6 mm	1.3 mm	6.5 mm
IPM (axially magnetized PMs)			
10.5 mm	23 mm	5.15 mm	7 mm
15 mm	25 mm	2.5 mm	10 mm
15 mm	27 mm	5.5 mm	10 mm
15 mm	27 mm	3 mm	10 mm
15 mm	34 mm	6.5 mm	10 mm

Highlighted geometry is the chosen design.

Fig. 4. Performance comparison of different mover geometries defined with Tab. II. The chosen design is highlighted in Tab. II.

However, since the final performance of the MALTA will depend strongly on the actual cooling performance, the thermal properties of the actuator will be studied experimentally in Sec. V-B. A winding fill factor of 0.6 is assumed based on earlier experience with electrical machines of similar size.

The performance of different mover geometries is shown in Fig. 4. This analysis shows the contradiction between the forces and accelerations, which is an expected behavior as more PMs in the mover guarantee higher flux density in the air gap and consequently higher forces. On the other hand, more PMs increase the mover mass and reduce the accelerations. A mover geometry that is a good compromise between high forces and high accelerations is chosen as the final mover design, which is the IPM mover topology that is denoted in Fig. 4 and its dimensions are highlighted in Tab. II.

B. Stator Design

A key aspect in the MALTA stator design is a trade-off between the achievable drive and bearing forces, and the radial pull force when the mover is radially displaced. The effect of two key geometrical parameters on this trade-off is studied, tooth thickness τ_t and tooth depth r_t, which are shown in Fig. 5(a). Since the start-up is the most critical for the MBs, i.e. requires the highest radial pull force, this scenario is used to determine the stator teeth size.

Two groups of 3D FEM simulations are performed for the MALTA in the scenario where the mover touches the touch-down bearing (Touch-down bearing is used in machines with MBs to avoid a damage of the mover or the stator in the case MBs stop working or are overloaded [21].). In one group the
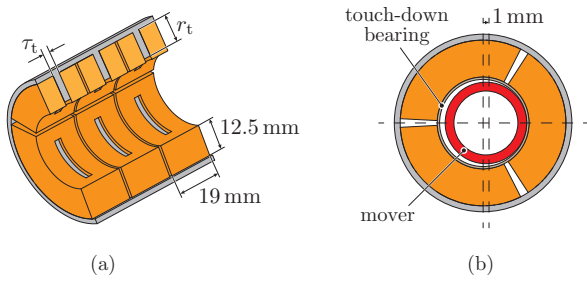
(a)   (b)

Fig. 5. (a) Cross section of the MALTA module with denoted teeth and size of the winding. (b) Stator teeth design scenario: mover displaced such that it touches the touch-down bearing ($1\,\mathrm{mm}$ displacement). The thickness of the touch-down bearing is $1\,\mathrm{mm}$.
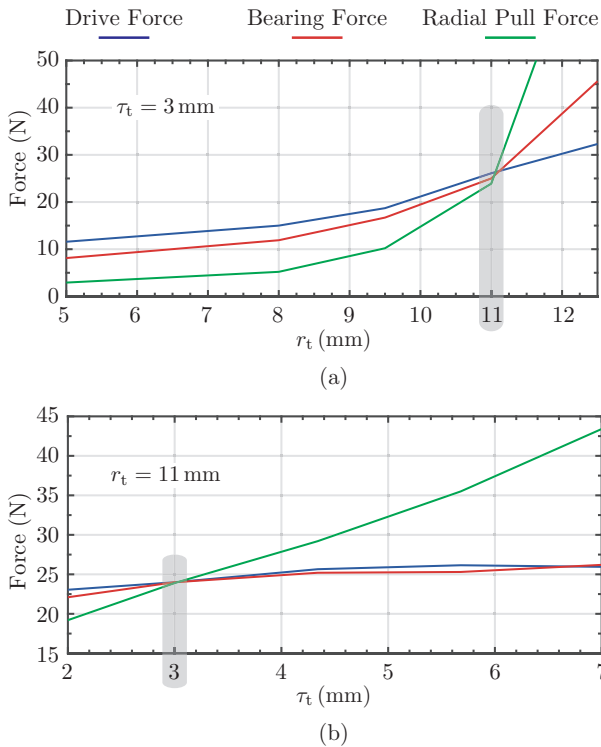

(a)

(b)

Fig. 6. Two groups of 3D FEM simulations that examine the influence of the tooth depth (r_t) and the tooth thickness (τ_t) on the drive, bearing and radial pull forces: (a) tooth thickness is constant, while tooth depth is swept, and (b) tooth thickness is swept, while tooth depth is constant.

tooth thickness τ_t has a fixed value and the tooth depth r_t is changed. In the other group, the tooth thickness τ_t is changed while the tooth depth r_t is fixed. The outer dimensions of the windings are fixed, see Fig. 5(a).

In the first group of simulations, the influence of the tooth depth on the drive, bearing and the radial pull forces is examined. If the tooth depth is equal to the radial size of the windings ($r_t = 12.5\,\mathrm{mm}$), the radial pull force is much higher than the continuous bearing force. In order to reduce the radial pull force, the tooth depth is reduced and its influence on the forces is shown in Fig. 6(a). As a consequence, the continuous drive and bearing forces are lower. The tooth depth of $r_t = 11\,\mathrm{mm}$ is chosen for the final design, since the pull
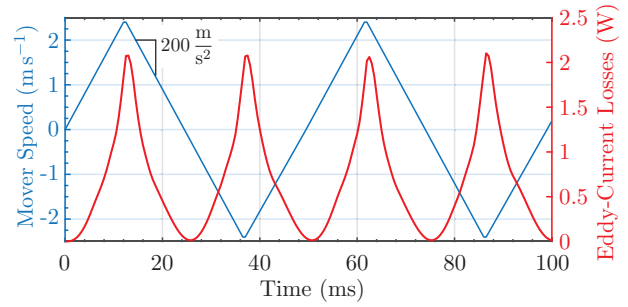

Fig. 7. Simulated eddy-current losses in the stator teeth and back iron for a speed profile (blue curve) in the extreme case where the mover accelerates and decelerates with $20g$ on the axial stroke of $30\,\mathrm{mm}$. The obtrained average eddy-current losses are $\approx 0.7\,\mathrm{W}$.

force is significantly reduced and close to the continuous bearing force.

In the second group of the simulations, see Fig. 6(b), the influence of the tooth thickness on the drive, bearing and radial pull forces is examined. Increasing the tooth thickness leads to an increased radial pull force, but results in no increase of the drive and bearing forces since the copper volume and hence the electric loading are decreasing. Therefore, the tooth thickness of $\tau_t = 3\,\mathrm{mm}$ is chosen for the final design.

Generally, in systems with short stroke movement the average speed is rather low. Consequently, eddy-current losses due to the PM movement are low compared to copper losses, which justifies building these systems from solid iron [22]. Additionally, this is shown once more here, using a worst case 2D FEM model.

Because of the transverse flux in the stator iron and complicated geometry, lamination is not considered. The stator is built of solid steel CK45, which magnetic properties are measured and reported in [23]. In order to check the order of eddy-current losses in the stator iron, a 2D FEM model is utilized, see Fig. 7. A very high axial acceleration of $20g$ is assumed. The acceleration is intentionally above what the machine can continuosly deliver, such that the eddy currents are calculated for the absolute worst case. The 2D FEM model is axis-symmetric, therefore the slits between the teeth of the MALTA are neglected, which is another worst-case approximation, as both the total flux and the eddy-current loop are larger. Hence, the eddy-current losses in the actual MALTA will be lower for the same speed profile. The average eddy-current losses are $0.7\,\mathrm{W}$, which is only $4.7\,\%$ of the assumed copper losses. Therefore, it is expected that the eddy-current losses will not have a significant influence on the temperature rise of the MALTA and will not worsen its performance.

IV. MALTA PROTOTYPE

A. Mover

The mover is of IPM type (see Fig. 3 on the right) and its geometrical parameters are highlighted in Tab. II. In the prototype, the PMs and the iron rings are stacked on a lightweight carbon rod, see Fig. 8. The total number of poles (iron rings) in the mover prototype is 10. Each module covers 4 poles (8 poles for the two modules) and the length of the 2
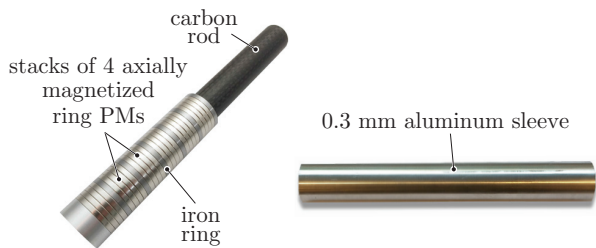
Fig. 8. Built mover prototype: axially magnetized ring PMs are stack on a light-weight carbon rod. Finally, the whole assembly is inserted into a $0.3\,\text{mm}$ thick aluminum sleeve that protects PMs. The smooth surface of the sleeve can be used for eddy current radial position sensing.

205 turns
0.6 electrical fill factor
0.5 mm wire diameter

Fig. 9. Built coil prototype of the MALTA winding, which schematic representation is shown in Fig. 2(b).

poles covers the stroke, such that a constant active length of the MALTA is kept during the operation.

The aluminum sleeve that shields the mover is used to protect the PMs from breaking if the touch-down bearing is hit. Additionally, the smooth conductive surface of the sleeve will be used in a next step for eddy-current radial position sensing [24].

B. Windings

A manufactured coil prototype is shown in Fig. 9. Its shape differs from the schematic representation of the MALTA winding from Fig. 2(b) due to manufacturing constraints. It is built using $0.5\,\text{mm}$ wire and consists $205\,\text{turns}$. The achieved fill factor is 0.6.

In order to determine the maximum expected voltage across the winding terminals, phase resistance and inductance are measured and the back emf is estimated from the 3D FEM simulation. In the simulation, a constant linear mover speed of $2\,\text{m}\,\text{s}^{-1}$ is assumed as a worst-case scenario, since $2\,\text{m}\,\text{s}^{-1}$ is the peak speed during the oscillating motion of the actuator. Accordingly, a peak induced back emf per turn of $26\,\text{mV}$ is obtained. The winding resistance and inductance are measured as $1.44\,\Omega$ and $2.14\,\text{mH}$, once the windings are inserted into the stator and the stator is potted. The measurement is taken at $66.7\,\text{Hz}$, which is the worst-case electrical frequency corresponding the mover's peak instantaneous linear speed of $2\,\text{m}\,\text{s}^{-1}$ (pole length is $15\,\text{mm}$).

The electrical loading of the windings is obtained from the stator design (see Sec. III), as $300\,\text{Ampere}-\text{turns}$. For 205 winding turns, this corresponds to a phase current amplitude of $1.46\,\text{A}$. Consequently, the amplitude of the phase voltage is estimated to be around $7.5\,\text{V}$, see Fig. 10. The peak-to-peak value of this voltage is $\approx 15\,\text{V}$, which implies that an inverter with $24\,\text{V}$ DC link voltage can be used to drive the actuator.
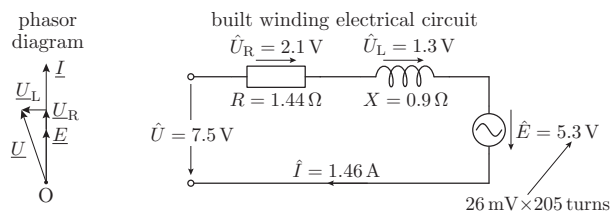

Fig. 10. Phasor diagram and electrical circuit of the built winding ($\underline{X}$ - phasor quantity; $\hat{X}$ - amplitude).
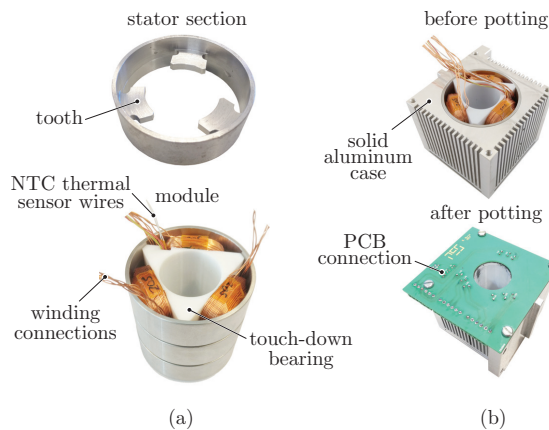

Fig. 11. (a) Stator section and module. (b) Module inside the aluminum case, before and after potting.

C. Stator

As already mentioned in Sec. III-B, the stator is built from solid steel. It is divided into three stator sections, one of which is depicted in Fig. 11(a). In order to monitor the temperature in the machine, three NTC thermal sensors are inserted in the radially innermost surface of one winding in each stator section. From the inner side, a 3D printed touch-down bearing is inserted, which protects mover and stator windings from damaging in case MBs stop working [21], and is furthermore used as a molt in the potting procedure.

In order to fix the module in the test bench, it is inserted into an aluminum case shown in Fig. 11(b). Further, the stator is potted with epoxy, which holds windings and stator sections together and ensures better cooling of the windings. A PCB connector is designed that gathers all $9 \times 2 = 18$ power winding connections and 6 connections for the three NTC thermal sensors.

D. Test Bench

A prototype of the MALTA is built in order to verify its concept and FEM models. As the mover is magnetically levitated, a verification of the actual system without closed loop control, sensors and power electronics is not possible. Therefore, a custom test bench shown in Fig. 12 is built, in which mechanical bearings are used to suspend the mover. The mechanical bearings are used only during the initial measurement and verification stage. Later on, they are removed and
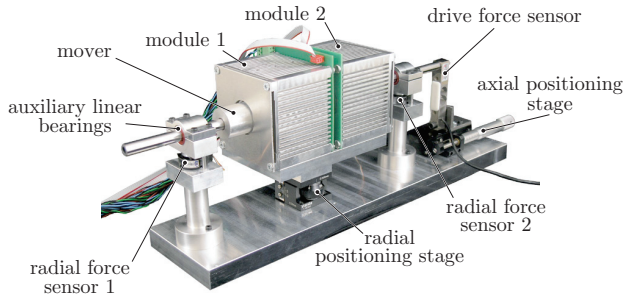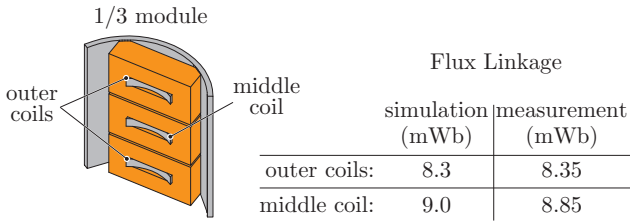
Fig. 12. MALTA test bench.

Fig. 13. Measured flux linkage of the outer and the middle coils in the MALTA module and its comparison to the 3D FEM simulation results.

MB are used in regular operation. The two radial force sensors, located beneath each linear bearing, are used to measure the bearing force. The drive force is measured with one sensor, which is attached to one end of the mover and to the axial positioning stage that is used for setting the axial position of the mover. The axial position of the modules (module 1 and module 2) is fixed, while its radial position is set with the radial position stage. The radial position of the mover is fixed. Sensors used in the measurements are given in Tab. IV in Appendix.

V. MEASUREMENT RESULTS

A. Flux Linkage

Flux linkage is obtained by integrating the induced back emf, which is measured across the open-circuited machine terminals while the mover travels its complete stroke back and forth several times, actuated manually. Obtained flux linkage values are given in Fig. 13. The flux linkage is lower in the outer coils than in the middle coils due to the flux leakage in the outer coils. 3D FEM simulation results for the flux linkage of the outer and the inner coils are provided and a good match with the measurements is achieved.

B. Temperature Rise

The continuous drive and bearing forces of the MALTA are limited by the maximum allowable winding temperature. So far, the electrical loading has been calculated according to a simplified thermal model presented in [20]. However, in order to asses the actual performance limit of the built prototype, a winding temperature rise measurement is performed for determining the actual thermal properties in detail, and consequently, for determining the maximum permissible electrical loading.
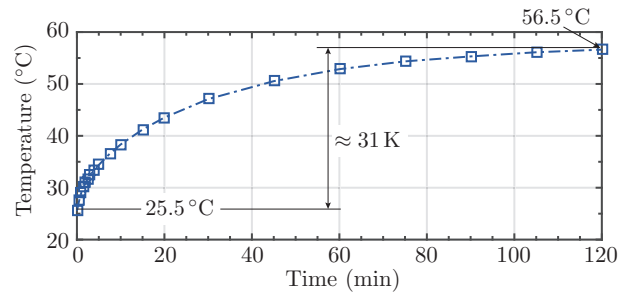

Fig. 14. Winding temperature rise measurement for $20.5\,\mathrm{W}$ of copper losses in the MALTA windings of a module.

At standstill, a DC voltage is applied to the windings and a total copper losses of $20.5\,\mathrm{W}$ are dissipated. Note that, this is an arbitrary value and is only used to estimate the thermal properties of the prototype. The measured winding temperature is shown in Fig. 14. The thermal resistance of the test bench setup, in which the MALTA is enclosed with an aluminum case, can be roughly estimated as $R_{\mathrm{th}} \approx 31\,°\mathrm{C}/20.5\,\mathrm{W} = 1.51\,°\mathrm{C}\,\mathrm{W}^{-1}$. Obtained thermal resistance of the test bench closely resembles the thermal properties of the MALTA in a real life application. The casing have fins and it is connected with the radial positioning stage to the aluminum plate, which resembles the MALTA that is held by a robot arm.

With the estimated thermal resistance of $R_{\mathrm{th}} \approx 1.51\,°\mathrm{C}\,\mathrm{W}^{-1}$, and a given maximum continuous winding temperature, the admissible continuous electrical loading of the MALTA can be calculated, which directly allows to specify its performance. Setting the maximum winding temperature to $100\,°\mathrm{C}$, continuous copper losses of $72\,°\mathrm{C}/1.51\,°\mathrm{C}\,\mathrm{W}^{-1} \approx 47\,\mathrm{W}$ are obtained. This value will be used in the following sections to specify the expected performance of the MALTA prototype.

C. Drive Force Constant

The MALTA drive force constant (drive force divided by the current amplitude) is determined in this subsection. The measurement is performed with one module. Hence, for the actual MALTA with two modules (module 1 and module 2, see Fig. 12), the drive force constant is doubled.

The electrical current vector and the mover flux vector in this measurement are at the fixed axial positions with $\pm\pi/2$ electrical angle distance. The electrical distance of these two vectors is determined as follows. A current vector axial position is fixed, e.g. at $\theta_{\mathrm{d}} = 7\pi/6$, which gives the following winding currents (see (1) and (2)):

$$\underline{I}^{\mathrm{d}} = I_{\mathrm{m}}^{\mathrm{d}} \begin{bmatrix} -\sqrt{3}/2 & 0 & \sqrt{3}/2 \\ -\sqrt{3}/2 & 0 & \sqrt{3}/2 \\ -\sqrt{3}/2 & 0 & \sqrt{3}/2 \end{bmatrix}. \tag{5}$$

The (column, row) position (j, k) in the matrix denote the current in the L_{jk} winding of the MALTA, see Fig. 2(b). In the following, the axial position of the mover is changed, e.g. in steps of $1\,\mathrm{mm}$, while the current vector $\underline{I}^{\mathrm{d}}$ in kept constant. The measured drive force is shown in Fig. 15(a).
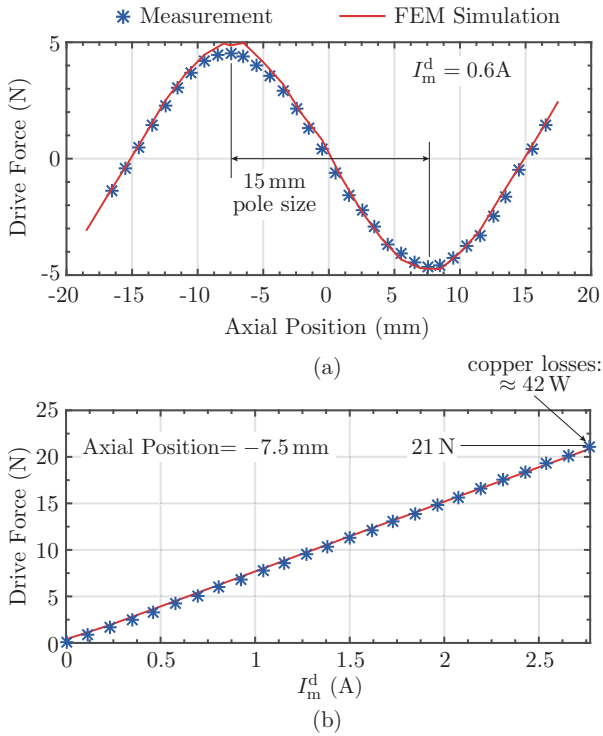
(a)

(b)

Fig. 15. Drive force constant measurement and comparison with FEM simulations: (a) Synchronization of the constant DC current vector given in (5) with the mover flux vector by changing the mover's axial position. (b) Drive force constant measurement by changing the DC current vector amplitude I_m^d for the fixed axial position of the mover at $-7.5\,\text{mm}$ that results in $\pi/2$ electrical distance between the DC current vector and mover flux vector.

The axial positions of the mover that give the $\pm\pi/2$ electrical distance between the current vector given with (5) and the mover flux vector are $\pm 7.5\,\text{mm}$. In the sense of the well known dq-transformation, direct current component is equal to zero at this positions, i.e. the force-per-copper-loss is maximized. Additionally, the $15\,\text{mm}$ pole size in the mover can be observed, which agrees with the designed mover pole size, see Tab. II.

In the next measurement the drive force constant is obtained. The axial position of the mover is fixed to $-7.5\,\text{mm}$, while the current vector amplitude I_m^d is changed, see Fig. 15(b). The drive force constant is estimated from the measurement as

$$K_d = \frac{\text{Axial Force}}{I_m^d} \approx 7.6\,\text{N}\,\text{A}^{-1}. \tag{6}$$

The drive force of $21\,\text{N}$ per module can be achieved with copper losses of $42\,\text{W}$ in continuous operation, see Fig. 15(b). The maximum continuous electrical loading with copper losses of $\approx 47\,\text{W}$ per module of the MALTA prototype is obtained in Sec. V-B. The drive force per module for this losses is $22.2\,\text{N}$. Therefore, the continuous drive force with two modules is $2 \times 22.2\,\text{N} = 44.4\,\text{N}$. The mass of the mover without the extension that is required solely for the temporary linear bearings is $0.35\,\text{kg}$, which results in an achievable continuous axial acceleration of the MALTA with two modules of $\approx \pm 12.5g$.
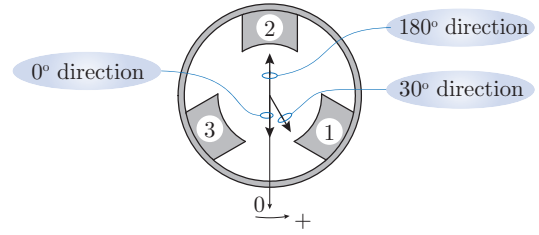

Fig. 16. Force circumferential position used in Fig. 17.

D. Bearing Force Constant

This measurement is conducted in a similar fashion as the drive force constant measurement, i.e. the current vector at fixed axial position is applied, its amplitude is changed and the bearing force is measured. In order to examine MB properties of the MALTA in circumferential direction an FEM simulation shown in Fig. 17(a) is conducted. In this simulation the bearing force direction is observed over different circumferential positions for a constant current amplitude, i.e. $I_m^b = 3\,\text{A}$ and $\varphi = [0°, \dots, 360°]$ in (4). Circumferential position of the MALTA stator is defined in Fig. 16. Three points from the plot, i.e. $0°$, $30°$ and $180°$ directions are investigated further with simulations and measurements such that bearing constants for each of these positions are determined.

In order not to generate any parasitic drive force, the bearing force is measured at $0\,\text{mm}$ axial position, see Fig. 15(a), which is electrically $90°$ away from the position where the drive force is measured.

The bearing force constant measurement for $0°$ direction is conducted in the following setup. The current vector with the same fixed axial argument as (5), which is $\theta_d = 7\pi/6$, and circumferential argument $\varphi = -\pi/3$, is set. This gives the following set of the currents in the windings:

$$\underline{I}^{b\text{-}0} = I_m^b \begin{bmatrix} -\sqrt{3}/4 & 0 & \sqrt{3}/4 \\ \sqrt{3}/2 & 0 & -\sqrt{3}/2 \\ -\sqrt{3}/4 & 0 & \sqrt{3}/4 \end{bmatrix}. \tag{7}$$

This vector is calculated using (4), where the circumferential phase j is denoted on the teeth in Fig. 16. The columns in the matrix of the current vector $\underline{I}^{b\text{-}0}$ belong to the circumferential positions denoted as ①, ② and ③ in Fig. 16. The amplitude I_m^b is changed and the bearing force is measured. In Fig. 17(b) this measurement is shown and compared to 3D FEM simulation results. From this measurement the bearing force constant for the $0°$ direction is calculated as

$$K_b^{0°} = \frac{\text{Bearing Force}}{I_m^b} \approx 5.6\,\text{N}\,\text{A}^{-1}. \tag{8}$$

Copper losses in the last measurement point are $\approx 28\,\text{W}$, see Fig. 17(b). According to the above described temperature rise measurements, copper losses of $\approx 47\,\text{W}$ can be continuously dissipated in the module. Consequently, a maximum continuous bearing force of $\approx 21.9\,\text{N}$ per module in the $0°$ circumferential direction shown in Fig. 16 can be achieved.

The second bearing force constant measurement is conducted for $30°$ direciton, see Fig. 16. Also here, the current vector has the same fixed axial position argument
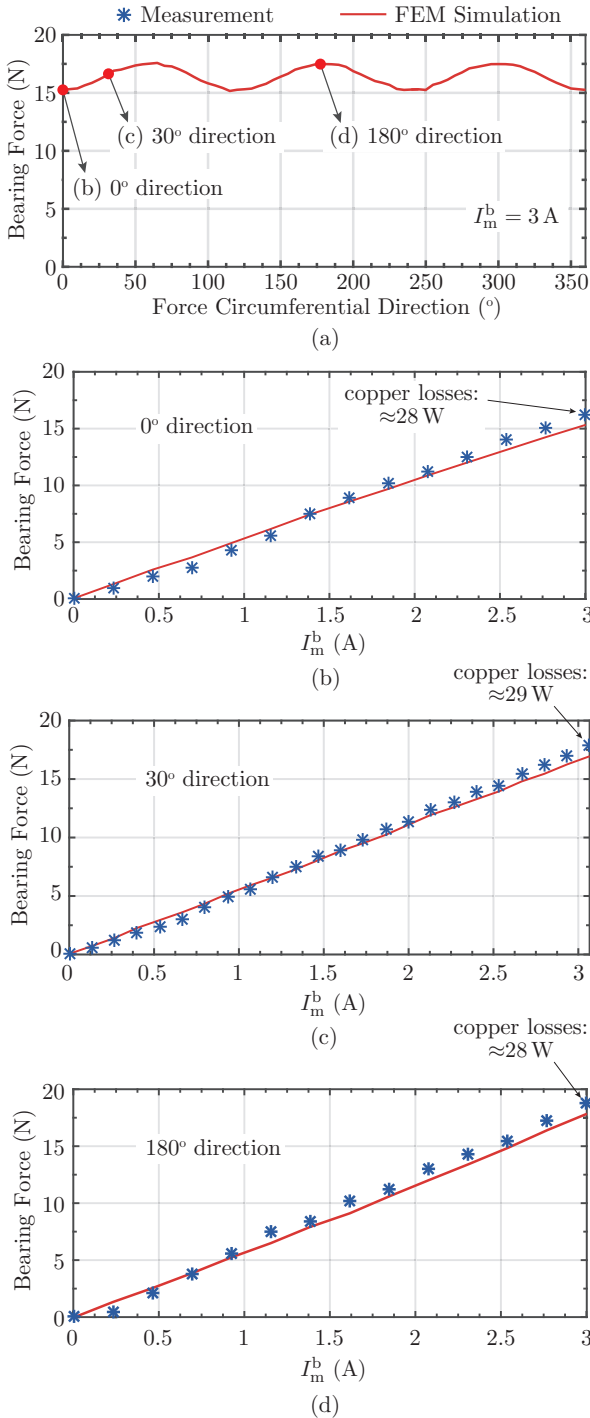
Fig. 17. Bearing force FEM simulations and measurements. (a) FEM simulation of the bearing force versus circumferential direction. Circumferential position is shown in Fig. 16. (b) Bearing force constant measurement for the $0°$ direction. (c) Bearing force constant measurement for the $30°$ direction. (d) Bearing force constant measurement for the $180°$ direction.

of $\theta_d = 7\pi/6$ and circumferential position argument of $\varphi = -\pi/6$, which results in the following current vector

$$\underline{I}^{\text{b-30}} = I_m^b \begin{bmatrix} -3/4 & 0 & 3/4 \\ 3/4 & 0 & -3/4 \\ 0 & 0 & 0 \end{bmatrix}. \tag{9}$$

Similar to $\underline{I}^{\text{b-0}}$, the columns in the matrix belong to the circumferential positions denoted as ①, ② and ③ in Fig. 16. The current amplitude is changed and the bearing force is measured, as shown in Fig. 17(c). From this measurement, the bearing force constant for 30° circumferential direction (see Fig. 16) is calculated as

$$K_b^{30°} = \frac{\text{Bearing Force}}{I_m^b} \approx 5.96\,\text{N A}^{-1}. \tag{10}$$

In the last measurement point the copper losses are $\approx 29\,\text{W}$, see Fig. 17(c). The maximum continuous bearing force for 30° direction of $23.2\,\text{N}$ per module is obtained assuming the copper losses of $47\,\text{W}$.

Bearing force constant measurement for 180° direction is conducted with the current vector direction opposite to $\underline{I}^{\text{b-0}}$, i.e. $\underline{I}^{\text{b-180}} = -\underline{I}^{\text{b-0}}$ and shown in Fig. 17(d). The measured bearing force constant is

$$K_b^{180°} = \frac{\text{Bearing Force}}{I_m^b} \approx 6.26\,\text{N A}^{-1}. \tag{11}$$

The maximum continuous bearing force for 180° direction of $24.4\,\text{N}$ per module can be generated assuming the copper losses of $47\,\text{W}$.

Bearing force constant depends on the bearing force circumferential direction, which is shown with FEM simulations in Fig. 17(a) and confirmed with measurements for 0°, 30° and 180° circumferential directions. Minimal measured bearing force constant $K_b^{0°}$ and the maximal one $K_b^{180°}$ differ for $\approx 11.8\,\%$.

Additionally, the bearing force constant depends on the radial displacement of the mover from its center position. This dependence is $\approx 2\,\text{N A}^{-1}/\text{mm}$ (per mm of the radial displacement). As typical radial displacements in MB machines of this size are in the range of several μm, consequently, the influence of the radial mover displacements in the levitation gap on the bearing force constant is very low.

An important aspect for the MALTA is decoupled control of the drive and bearing forces, which is achieved by proper shaping of phase currents (see Sec. II). Measurements and FEM simulation results in Fig. 18 show that the cross coupling between the drive and the bearing forces is negligible when bearing force is commanded. Negligible cross coupling between the forces when the drive force is commanded is clear as it reduces MALTA operation to the standard TLA in which the bearing force is always zero.

E. Radial Pull Force

The radial pull force measurement for one module is shown in Fig. 19 and compared with 3D FEM magnetostatic simulation results. This measurement is important for the self-bearing operation of the MALTA, since it will act as radial position disturbance if the mover is not in the center
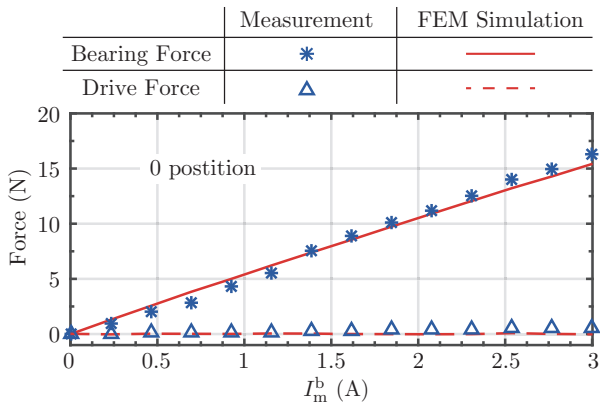
Fig. 18. Measurements and FEM simulations that show decoupled control of the drive and bearing forces, when the bearing force is commanded.
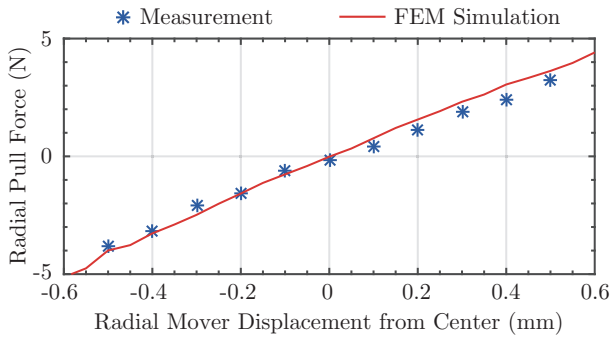

Fig. 19. Radial pull force measurement and comparison with 3D FEM magnetostatic simulation results when the mover is displaced from its center position.

position. Additionally, if the mover is continuously displaced for $\approx 0.5\,\mathrm{mm}$, the radial pull force would have to be balanced by MB force, which will raise copper losses per module up to $\approx 2.5\,\mathrm{W}$.

F. MALTA Performance

The MALTA performance with the two modules is determined in this section. These results rely on the measurements of the temperature rise (see Sec. V-B), drive force constant (see Sec. V-C) and bearing force constant (see Sec. V-D) of one module.

The MALTA performance is summarized in Tab. III. The mass of the mover is $0.35\,\mathrm{kg}$ without the extension that is required solely for the temporary linear bearings.

VI. CONCLUSION

Tubular linear actuators (TLAs) can realize linear reciprocal motion as a direct drive, i.e. no mechanical transmissions are needed like in the conversion from rotational to translational motion. Therefore, higher compactness and efficiency can be achieved with TLAs in systems with linear reciprocal motion.

Standard bearings used in TLAs are either mechanical bearings or air bearings. These bearings feature drawbacks such as friction, risk of contamination due to wear or limited

TABLE III
MALTA PERFORMANCE WITH TWO MODULES. FOR 0°, 30° AND 180° DIRECTIONS SEE FIG. 16.

Quantity	Value
continuous drive/axial/thrust/linear force	44.4 N
continuous bearing force, 0 position	43.7 N
continuous bearing force, 30° position	46.4 N
linear/axial acceleration	12.5g
sustainable radial acceleration, 0° direction	12.5g
sustainable radial acceleration, 30° direction	13.3g
sustainable radial acceleration, 180° direction	13.9g

lifetime of the mechanical bearings, increased system volume and complexity due to pressurized air supply for air bearings. Furthermore, operation in low pressure environments is not possible for air bearings. These issues can be avoided if magnetic bearings (MBs) are used in TLA systems. MBs could be used as two separate machines on each axial side of the TLA, which would increase its length and complexity. Therefore, in this paper, a novel self-bearing (bearingless) TLA is analyzed, resulting in a magnetically levitated tubular actuator (MALTA). The outer dimensions of the stator, i.e. active length and diameter, are $120\,\mathrm{mm}$ and $50\,\mathrm{mm}$, respectively. Flux linkage measurement, drive, bearing and radial pull forces measurements are shown and good agreement with FEM simulations is achieved. The maximum feasible drive force in continuous operation is $\approx 44\,\mathrm{N}$ and a maximum axial acceleration of $\approx 12.5g$ can be achieved in continuous operation. This force is roughly $40\,\%$ lower compared to a standard TLA, because in the standard TLA the flux linkage is higher as there are no slits in the teeth.

Further work will include axial and radial position sensor development and closed-loop control system design. The control system in the first step will be implemented by means of feedback axial and radial position controllers in cascaded structure and stationary coordinates. The control system will also include a feedforward loop, for which the dynamic model of the mover will be derived in the subsequent works.

APPENDIX

Tab. IV in this section includes the information about the sensors employed in the test bench.

TABLE IV
SENSORS USED IN THE TEST BENCH.

Measurement	Manufacturer / Model
temperature sensor	see [25]
drive force sensor	see [26]
bearing force sensor	see [27]

REFERENCES

[1] I. Boldea, *Linear Electric Machines, Drives, and MAGLEVs Handbook.* CRC Press, 2013.

[2] J. Paulides, L. Encica, K. Meessen, and E. Lomonova, "Fast Component Placement with Optimized Long-Stroke Passive Gravity Compensation Integrated in a Cylindrical/Tubular PM Actuator," in *Proc. of International Conference on Electrical Machines and Systems*, vol. 2, no. 3, pp. 275–282, 2013.

[3] E. A. Baran, T. E. Kurt, and A. Sabanovic, "Lightweight Design and Encoderless Control of a Miniature Direct Drive Linear Delta Robot," in *Proc. of 8th International Conference on Electrical and Electronics Engineering (ELECO)*, pp. 502–506, 2013.

[4] F. Bechet, K. Ogawa, E. Sariyildiz, and K. Ohnishi, "Electrohydraulic Transmission System for Minimally Invasive Robotics," *IEEE Transactions on Industrial Electronics*, vol. 62, no. 12, pp. 7643–7654, 2015.

[5] Y. Nakajima, T. Nozaki, and K. Ohnishi, "Heartbeat Synchronization with Haptic Feedback for Telesurgical Robot," *IEEE Transactions on Industrial Electronics*, vol. 61, no. 7, pp. 3753–3764, 2014.

[6] J. Wang, W. Wang, and K. Atallah, "A Linear Permanent-Magnet Motor for Active Vehicle Suspension," *IEEE Transactions on Vehicular Technology*, vol. 60, no. 1, pp. 55–63, 2011.

[7] V. DelliColli, P. Cancelliere, F. Marignetti, R. DiStefano, and M. Scarano, "A Tubular-Generator Drive for Wave Energy Conversion," *IEEE Transactions on Industrial Electronics*, vol. 53, no. 4, pp. 1152–1159, 2006.

[8] J. Wang, W. Wang, G. W. Jewell, and D. Howe, "A Low-Power, Linear, Permanent-Magnet Generator/Energy Storage System," *IEEE Transactions on Industrial Electronics*, vol. 49, no. 3, pp. 640–648, 2002.

[9] J. Wang, M. West, D. Howe, H. Zelaya-De La Parra, and W. M. Arshad, "Design and Experimental Verification of a Linear Permanent Magnet Generator for a Free-Piston Energy Converter," *IEEE Transactions on Energy Conversion*, vol. 22, no. 2, pp. 299–306, 2007.

[10] I. Boldea, L. Tutelea, W. Xu, and M. Pucci, "Linear Electric Machines, Drives and MAGLEVs: An Overview," *IEEE Transactions on Industrial Electronics*, vol. PP, no. 99, pp. 1–1, 2017.

[11] J. Latham, M. L. McIntyre, and M. Mohebbi, "Parameter Estimation and a Series of Nonlinear Observers for the System Dynamics of a Linear Vapor Compressor," *IEEE Transactions on Industrial Electronics*, vol. 63, no. 11, pp. 6736–6744, 2016.

[12] J. Wang, D. Howe, and Z. Lin, "Design Optimization of Short-Stroke Single-Phase Tubular Permanent-Magnet Motor for Refrigeration Applications," *IEEE Transactions on Industrial Electronics*, vol. 57, no. 1, pp. 327–334, 2010.

[13] G. Zhong, H. Deng, G. Xin, and H. Wang, "Dynamic Hybrid Control of a Hexapod Walking Robot: Experimental Verification," *IEEE Transactions on Industrial Electronics*, vol. 63, no. 8, pp. 5001–5011, 2016.

[14] J. Zhang, W. Li, J. Yu, Q. Zhang, S. Cui, Y. Li, S. Li, and G. Chen, "Development of a Virtual Platform for Telepresence Control of an Underwater Manipulator Mounted on a Submersible Vehicle," *IEEE Transactions on Industrial Electronics*, vol. 64, no. 2, pp. 1716–1727, 2017.

[15] LinMot. Stainless Steel Motors . Accessed: 22/08/2017. [Online]. Available: http://www.linmot.com/products/stainless-steel-motors/

[16] J. J. Paulides, J. L. Janssen, and E. A. Lomonova, "Bearing Lifetime of Linear PM Machines," in *Proc. of IEEE International Energy Conversion Congress and Exposition (ECCE USA)*, pp. 1083–1090, 2009.

[17] N.-C. Tsai and C.-W. Chiang, "Design and Analysis of Magnetically-Drive Actuator Applied for Linear Compressor," *Mechatronics*, vol. 20, no. 5, pp. 596–603, 2010.

[18] G. Krebs, A. Tounzi, B. Pauwels, D. Willemot, and F. Piriou, "Modeling of a Linear and Rotary Permanent Magnet Actuator," *IEEE Transactions on Magnetics*, vol. 44, no. 11, pp. 4357–4360, 2008.

[19] P. Jin, H. Lin, S. Fang, and S. Ho, "Decoupling Control of Linear and Rotary Permanent Magnet Actuator Using Two-Directional d-q Transformation," *IEEE Transactions on Magnetics*, vol. 48, no. 10, pp. 2585–2591, 2012.

[20] S. Mirić, A. Tüysüz, and J. W. Kolar, "Comparative Evaluation of Linear-Eotary Actuator Topologies for Highly Dynamic Applications," in *Proc. of IEEE International Electric Machines and Drives Conference (IEMDC)*, pp. 1–7, 2017.

[21] H. Bleuler, M. Cole, P. Keogh, R. Larsonneur, E. Maslen, Y. Okada, G. Schweitzer, A. Traxler *et al.*, *Magnetic Bearings: Theory, Design, and Application to Rotating Machinery*. Springer Science & Business Media, 2009.

[22] K. J. Meessen, "Electromagnetic Fields and Interactions in 3D Cylindrical Structures: Modeling and Application," Ph.D. dissertation, Dept. Electric Eng., Eindhoven University of Technology, the Netherlands, 2012.

[23] M. Flankl, A. Tüysüz, and J. W. Kolar, "Impact of Iron Dust on Electromechanical Systems: A Case Study," in *Proc. of IEEE Annual Southern Power Electronics Conference (SPEC)*, pp. 1–8, 2016.

[24] C. M. Zingerli, P. Imoberdorf, J. W. Kolar, and T. Nussbaumer, "Rotor Position Measurement for a Magnetically Levitated 500'000 rpm Permanent Magnet Machine," in *Proc. of IEEE International Energy Conversion Congress and Exposition (ECCE USA)*, pp. 1778–1784, 2011.

[25] EPCOS - TDK, "NTC thermistors for temperature measurement, B57550G1 Datasheet," 2016.

[26] Messtechnik Schaffhausen GmbH, "LFP-19-10kg Datasheet," 2017.

[27] TE Connectivity Measurement Specialties, "FX1901 Compression Load Cell Datasheet," 2017.

Spasoje Mirić received the B.Sc. and M.Sc. degrees in electrical engineering in 2012 and 2013, respectively, from the University of Belgrade, Belgrade, Serbia. He is currently working towards his Ph.D. degree in electrical engineering at the Swiss Federal Institute of Technology (ETH) Zurich, Zurich, Switzerland. His research interests are novel electrical machine topologies, linear machines and bearingless motors for highly dynamic actuator systems.

Pascal Küttel received the B.Sc. and M.Sc. degrees in mechanical engineering in 2015 and 2017, respectively, from the Swiss Federal Institute of Technology (ETH) Zurich, Zurich, Switzerland. He did an internship at Maxon Motor AG, Sachseln, Switzerland, for six months. He is currentlly with EnDes Engineering and Design AG, as a mechanical engineer, working on the design and automation.

Arda Tüysüz received his B.Sc. degree in electrical engineering from Istanbul Technical University, Istanbul, Turkey, in 2006, his M.Sc. degree in electrical power engineering from RWTH Aachen University, Aachen, Germany, in 2009, and his Ph.D. degree in electrical drives from the Swiss Federal Institute of Technology (ETH) Zurich, Zurich, Switzerland, in 2015. His research interests during this period included novel electrical machine topologies, self-sensing control of high-speed electrical machines, electrical drives with very high signal-to-noise ratio and wide-bandgap power devices for very efficient and compact electrical drive systems. He is currently with ABB Corporate Research Center in Ladenburg, Germany.

Johann W. Kolar (F'10) received his M.Sc. and Ph.D. degree (summa cum laude / promotio sub auspiciis praesidentis rei publicae) from the University of Technology Vienna, Austria, in 1997 and 1999, respectively. Since 1984, he has been working as an independent researcher and international consultant in close collaboration with the University of Technology Vienna, in the fields of power electronics, industrial electronics and high performance drives. He has proposed numerous novel PWM converter topologies, and modulation and control concepts and has supervised over 70 Ph.D. students. He has published over 650 scientific papers in international journals and conference proceedings, 4 book chapters, and has filed more than 160 patents. The focus of his current research is on ultra-compact and ultra-efficient SiC and GaN converter systems, wireless power transfer, solid-state transformers, power supplies on chip, and ultra-high speed and bearingless motors. Dr. Kolar has received 26 IEEE Transactions and Conference Prize Paper Awards, the 2014 IEEE Middlebrook Award, the 2016 IEEE William E. Newell Power Electronics Award, the 2016 IEEE PEMC Council Award and two ETH Zurich Golden Owl Awards for excellence in teaching. He initiated and/or is the founder of four ETH Spin-off companies. He is a member of the steering committees of several leading international conferences in the field and has served from 2001 through 2013 as an Associate Editor of the IEEE Transactions on Power Electronics. Since 2002 he also is an Associate Editor of the Journal of Power Electronics of the Korean Institute of Power Electronics and a member of the Editorial Advisory Board of the IEEJ Transactions on Electrical and Electronic Engineering.